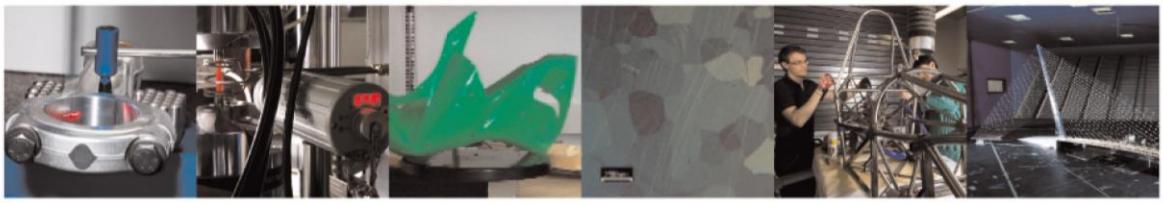

Insight into the effect of different thermal treatment routes on the microstructure of AlSi7Mg produced by laser powder bed fusion

R. Casati, M. Coduri, S. Checchia, M. Vedani

This is a post-peer-review, pre-copyedit version of an article published in journal title. The final authenticated version is available online at: https://doi.org/10.1016/j.matchar.2021.110881

Insight into the effect of different thermal treatment routes on the microstructure of AlSi7Mg produced by laser powder bed fusion

R. Casati[a,*], M. Coduri[b,c], S. Checchia[b], M. Vedani[a]

[a] Department of Mechanical Engineering, Politecnico di Milano, Via G. La Masa, 1, 20156, Milano (Italy)

[b] ESRF, European Synchrotron Radiation Facility. 71, avenue des Martyrs, 38000, Grenoble, France

c Department of Chemistry, University of Pavia, Via Taramelli 12, 27100, Pavia, Italy

* corresponding author: riccardo.casati@polimi.it

Abstract

The present work gives an insight into the microstructure evolution of AlSi7Mg produced by laser powder bed fusion and subjected to different heat treatment routes. Synchrotron powder diffraction and diffraction contrast tomography coupled with scanning and transmission electron microscopy investigations allowed an in-depth understanding of the effect of rapid solidification induced by laser powder bed fusion on material structure. In addition, the effects of solution treatment followed by water quenching and artificial aging and that of direct aging from the as built condition was investigated. The as built material exhibits the most important lattice contraction and the lower amount of Si phase, thus suggesting a higher content of solute Si, which decreases after artificial aging and after solution treatment. The eutectic Si is found in nanometric form, with crystallites of about 10 nm in size, which grow significantly after solution treatment. A similar behavior is also observed for the second phase β-Al_5FeSi. Traces of the π−$Al_8FeMg_3Si_6$ were observed after solution treatment. Direct aging induced the formation of a fine dispersion of β'' precipitates in the primary Al solidification cells, which is responsible for material hardness and strength increase. The thermal treatments strongly affect the residual macrostrain, which is higher for the as built material and decreases after aging and solution treatment. This was confirmed by diffraction contrast tomography, which provided a spatial resolved structural information and was used as alternative tool to quantify the distribution of Si and Al phases.

Introduction

Laser Powder Bed Fusion (L-PBF) is a powder bed additive manufacturing (AM) technology used to produce customized or complex-shape metal parts for functional and structural applications. Al-Si-Mg casting grades are the most used Al alloys for L-PBF, because they are not susceptible to hot-cracking and can be easily processed to generate objects with low residual porosity [1]. In particular, the AlSi7Mg alloy (A357 cast grade) is widely used because of its good corrosion resistance and mechanical performance. The AlSi7Mg

alloy is commonly reinforced by isothermal aging, which promotes the precipitation of the $Mg_4Al_3Si_4$ phase, known as β", from a supersaturated solid solution (SSSS). The full precipitation sequence from SSSS to equilibrium β phase is well accepted and abides the following steps:

4α-Al (SSSS) → atomic clusters → GP zones → β" → β', U1 (Type A), U2 (Type B), B' (Type C) → β [2-4]

Furthermore, Si particles can also form from the Al SSSS during aging.

In recent years, several scientific papers on microstructure and mechanical properties of Al-Si-Mg alloys produced by L-PBF have been published. Most of them focusses on the AlSi10Mg alloy, and only a small fraction investigated the AlSi7Mg alloy (corresponding to A357 grade) [5, 6-14].

The research works published on L-PBF of AlSi7Mg focus on optimization of process parameters [6], properties of lattice structures [7], thermal and mechanical fatigue properties [8,9,10], fracture toughness [11] and corrosion behavior of the alloy [12]. A few works investigated the effect of different heat treatment schedules on mechanical properties of A357 alloy [5,13,15]. Wang et al. investigated the effect of stress relief heat treatment on residual stresses and coarsening of microstructural features [15], whereas Casati et al. [5] and Van Cauwenbergh et al. [13] studied the effect of direct aging (T5 temper) on material properties. T5 temper allowed achieving higher material hardness and strength with respect to that attained by T6 temper (solution annealing followed by water quenching and artificial aging to peak hardness). A summary of the tensile properties of the AlSi7Mg alloy in as built, solution treated, T5 and T6 conditions is shown in Table 1.

The present work is aimed at giving an insight into the microstructure evolution of the AlSi7Mg produced by L-PBF and heat treated according to different strategies. An in-depth investigation of microstructural features of the alloy produced by L-PBF is needed to shed light on the effects of rapid solidification and post-processing heat treatments on mechanical properties. To this purpose, analyses of material microstructure by Field Emission Scanning Electron Microscopy (FE-SEM), Transmission Electron Microscopy (TEM) and X-Ray Diffraction (XRD) have been performed. Moreover, high resolution (HR) XRD, which allow to extract very accurate lattice parameters, was employed to estimate the solubility of Si into Al, and rediscuss the approach used in the literature. Eventually, traces of second phases were identified by high intensity (HI) XRD, otherwise undetectable through conventional laboratory diffractometers.

The present work is aimed also at evaluating the effect of different annealing routes on residual strain of 3D printed AlSi7Mg. The effect of thermal treatments on stress relaxation in AlSi7Mg was investigated in [15], while an analytical description of residual stresses is given in [16]. Residual stress analysis is generally performed by monitoring the d-space evolution with the specimen orientation, providing an information averaged over the specimen surface. To gain a spatial-resolved information, here we applied diffraction contrast tomography for the first time on AlSi7Mg. Indeed, previous X-ray tomography investigations have

been based on absorption contrast focused on the 3D distribution of pores [17] or defects [18] and their effect on fatigue behavior of the material.

Table 1. Mechanical properties of AlSi7Mg in different conditions (data from [5]).

	UTS [MPa]	**YS [MPa]**	**ε_R (%)**	**HV**
As built	398	257	7.6	102
Solution treated	n.a.	n.a.	n.a.	78
T5 temper	411	309	4.8	137
T6 temper	306	256	4.7	113

Materials and experimental methods

A Renishaw AM250 L-PBF system fitted with a 200 W single mode fiber laser was employed to produce a set of AlSi7Mg *alloy* (composition in wt.%: Si=6.5wt.%, Mg=0.58wt.%, Fe=0.1wt.%, Cu<0,05wt.%, Mn<0,1 wt.%, N<0,2 wt.%, O=0,1 wt.%, Al=bal.) cylindrical samples with diameter of 10 mm and height of 30 mm, using gas-atomized powder with particle size within the range of 20–63 µm.

Laser melting was performed by discrete and partially overlapped laser spots under Ar atmosphere. The following process parameters were set: hatch distance = 115 µm, point distance = 80 µm, exposure time = 140 µs, focal point = 1 mm (above the powder bed), layer thickness = 25 µm, power = 200 W. The samples were produced using a meander scanning strategy and the scanning direction was rotated by 67° after each layer completion. The job was performed without heating the build platform. Optimized parameters led to an average bulk density of 99.69% [5].

Solution annealing was performed at 540 °C for 1 h and it was followed by water quenching. Isothermal aging was performed at 160 °C for 4 h in order to achieve the peak-hardness condition according to the results reported in ref. [5]. The as built samples were stored at −18 °C before thermal treatments to limit natural aging. Alloy microstructure was investigated in the following conditions: as built (AB), directly aged from as built (T5 temper), solution treated and water quenched (ST) and solution treated, water quenched and aged (T6 temper).

All the specimens for XRD investigation were cut from central part of L-PBF process cylinders, machined and grinded into pieces with square section with side of about 1.5 mm and height of 30 mm. XRD data were collected at the High Resolution Powder Diffraction beamline (ID22) of the ESRF [19, 20] in high resolution and high intensity modes. The HR-XRD setup, using nine scintillators preceded by Si 111 crystal analyzers, was employed to achieve accurate determination of lattice parameters and suppression of parasitic scattering. HR-XRD patterns were collected summing continuous scans with 45 min total acquisition time for each sample, with al channels overlapping from 0 to 35 in 2θ, recording intensities every 15 ms. HI-XRD data were collected with a 2D Perkin Elmer detector, placed at 1 m from the sample, summing frames for about 20 minutes per sample to resolve small peaks from the background and attain statistically reliable data. 2D images were integrated using pyFAI software [21]. The specimens were rotated during acquisition to increase statistical averaging of crystallites. Incident wavelength was set to 0.35434 Å (~35 keV) for both experiments to reduce sample absorption. In order to assess a spatially resolved structural information, XRD-CT measurements were taken at the ESRF ID15A beamline [22] with an incident X-ray wavelength of 0.1305 Å (95 keV) focused to a spot size of 50 µm x 50 µm. The free-standing samples were mounted on a goniometer head on a high precision translation/rotation stage (Aerotech) and translated vertically over 10 steps of 25 µm to probe successive horizontal sections of the sample. Each section was recorded in 61 angular points between 0° and 180°, whereby the sample was translated over 2.25 mm in 50 steps. 2D diffraction images were collected by a Pilatus3 X CdTe 2 M detector (Dectris) in 10 ms exposures. Images were applied a 10% trimmed mean filter to remove intensity outliers before being integrated to 1D patterns [23]. Data processing and reduction was done using the programs nDTomo and pyFAI [21,24]. The final XRD-CT data volumes were reconstructed using the filtered back projection algorithm.

TEM analysis was carried out using a Philips CM12 transmission electron microscope operating at 120 kV and equipped with an energy-dispersive X-ray spectroscopy system. Samples were grinded to about 30 µm in thickness by abrasive papers and then polished with diamond paste and silica suspension. Final thickness reduction was achieved by ion milling. FE-SEM observations were carried out by Zeiss Sigma 500, equipped with energy dispersive X-ray spectroscopy analysis, secondary electrons and back-scattered electrons detectors. Light optical microscope (LOM) analysis was performed by Nikon Eclipse LV150NL. Samples for FE-SEM and LOM investigations were prepared by standard grinding and polishing procedure. Chemical and electrolytic etching were performed in order to reveal different microstructural features, using Keller's, Weck's and Barker's reagents.

Results and discussion

HR-XRD and HI-XRD analyses

Figure 1a depicts a portion of the HI-XRD patterns of the alloy in the as built condition and treated according to the different procedures. The figure highlights the change in the intensity of the Si peaks with the different annealing routes. A careful observation of the patterns (Figure 1b) also reveals that the AB and T5 specimens have much broader Si peaks than those of α-Al, suggesting a very limited crystallite size for the Si phase.

The corresponding crystallite sizes, estimated through Williamson-Hall (WH) approach [25], are in the order of 10 nm (see Table 2). The superlorentzian shape of the Si reflection (broad tail, sharp peak) might reflect a bimodal, or more complex, size distribution. Conversely, the breadths of the Si peaks of the two materials involving high-temperature solution treatment, namely ST and T6 samples, are similar to those of Al peaks, confirming crystallite coarsening to a size within the submicrometre or micrometre scale, excessively coarse to be accurately quantified through powder diffraction methods.

The high brilliance of the X-ray beam allowed to detect second phases from the background. Figure 1c highlights a low angle region, where a number of observed diffraction peaks do not correspond to any Si or Al phases. It should be noted that after background subtraction, the amplitude of the mean secondary peaks is about 4 counts against ~$13 \cdot 10^3$ counts of the (111) Al, meaning a very low volume fraction of the related second phases. Among these, the ternary Al_5FeSi, usually named β [26] (not to be confused with Mg_2Si, also known as β–phase) is observed in all the specimens. β–Al_5FeSi phase is less evident in the AB and T5 samples due to its nanometric dimension (broader peaks). Like Si, it grows to a micrometric size only after high temperature annealing. In ST and T6 samples, further reflections are observed, corresponding to the $Al_8FeMg_3Si_6$ (π-phase). However, the amount of π intermetallic is so small that it is not possible to ascertain its presence in nanometric form in AB and T5 samples.

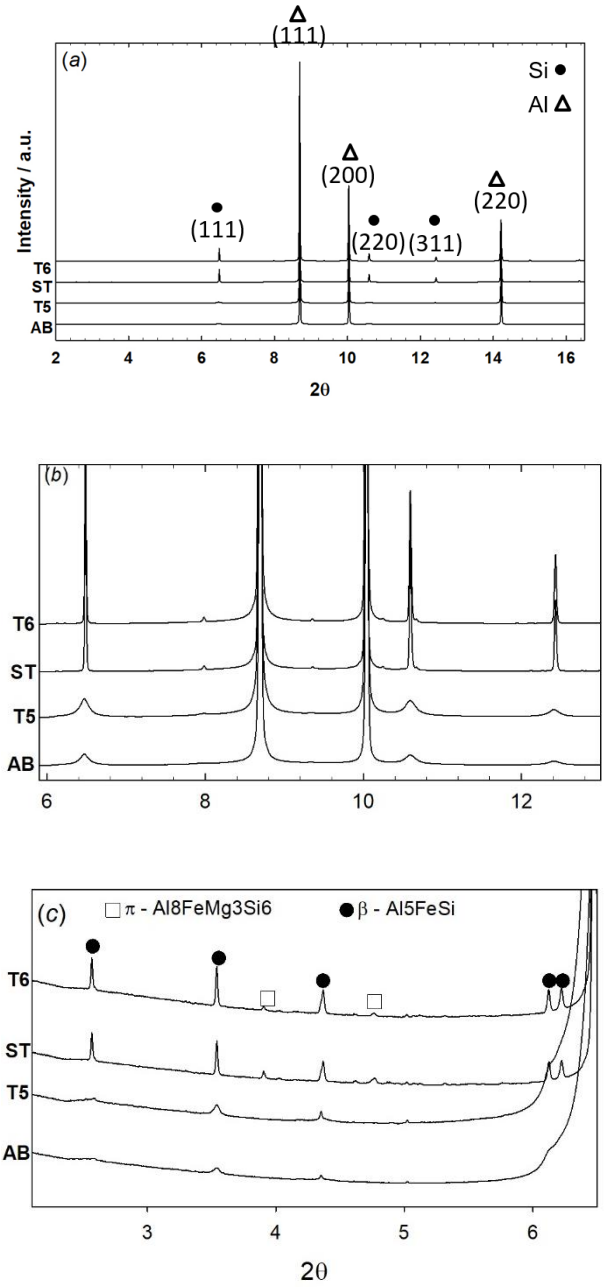

Figure 1. HI-XRD experimental patterns: (a) overview of Al and Si phases, (b) main Si peaks, and (c) focus on low angle background where the signal of other second phases is noticeable.

The formation of a solid solution in the AB sample results in the cell contraction of the α-Al phase (see Table 2), as the atomic radius of Si is smaller than that of Al [27]. Indeed, the lattice parameter of the AB alloy (0.40494 nm) is smaller than that of reference Al (0.40515 nm). In general, *a* decreases proportionally to the fraction of solute Si (i.e. the degree of saturation). In addition, a specimen containing 10% of Si and produced with the same process led to an even smaller unit cell (0.40483 nm) [28].

Table 2. Lattice parameters of the Al and Si phases, size of Si crystallites, Al macro-strain (200) and phase wt.% fraction of Si phase estimated via Rietveld refinements of different datasets. See main text for details and estimated standard deviations.

Sample	*a* Al (nm)	*a* Si (nm)	Si Crystallite Size (nm)	Al Macro-strain (200)	*wt.*% Si		
					HR-XRD	HI-XRD	XRD-CT
AB	0.404936(2)	50.54322(6)	9(2)	2.88E-04	6.0	2.9	3.5
T5	0.404979(2)	0.54323(5)	10(2)	1.60E-04	6.9	4.3	4.7
ST	0.405172(2)	0.542776(4)	coarse	1.36E-04	7.0	5.6	5.9
T6	0.405174(2)	0.542742(4)	coarse	1.04E-04	7.1	5.5	6.0

Many research works were previously conducted to investigate the solubility of Si into Al. Bendijk et al. [29] addressed the issue of relating lattice parameters to Si solubility in binary Al-Si alloys, taking data from solid state quenching up to 0.93 at.% Si. The following equation has been proposed:

$a = 0.40491 - 0.0174X_{Si}$ eq. (1)

which was modified with a second order term based on the behaviour of other binary intermetallics [30]. This is far different from the Vegard's law that one could extract by considering a hypothetical solid solution from Al to the equivalent FCC lattice parameter of Si (0.3731 nm [29]):

$a= 0.40491 - 0.0032X_{Si}$ eq. (2)

It turns out that, depending on the model adopted, one can have a factor of 2 in the estimated Si solubility. Either eq. (1) or (2) are routinely employed to estimate the Si content in Al-Si-Mg alloys, even though Mg is known to expand Al unit cell [31-33]. To this purpose, Marola et al. [27] proposed to move the intercept of eq. (1) to 0.40515 nm, which is defined as the equilibrium lattice parameter for the AlSi10Mg alloy, leading to:

$a = 0.40515 - 0.0174X_{Si}$ eq. (3)

It should be noted that variations in lattice parameters induced by Si or annealing are often less than 0.001 nm. Such a tiny extent is comparable with instrumental uncertainties (zero error, sample displacement) which are typical of laboratory instruments. In addition, peak shifts from residual stress can add further uncertainties to lattice parameters. This poses serious concerns on the reliability of some published data.

In this work, we determined accurate lattice parameters from HR-XRD. Applying the empirical eq. (3), we analytically attained 1.2% solute Si for AB, 1.0% for T5 and a slight negative value (<-0.1%) for the solution treated specimens, indicating no solubility.

The concentration of Si phase obtained by Rietveld refinement of HR-XRD data, reported in Table 2, qualitatively follows this trend. Indeed, assuming that the amount of Si forming the hardening precipitates (e.g. β'') is negligible, due to their small size and volume fraction, the larger the amount of solute Si, the smaller the amount Si phase. However, it turns out that for specimen T5, the sum of solute Si and Si phase adds up to 7.9 %, which significantly exceeds the nominal Si content. The uncertainty of wt.% Si computed by Rietveld refinements of HR-XRD patterns is about 0.2 %; however, changes in the refinement strategy led to systematic variations in the order of 1%, which should be taken as a more realistic uncertainty. The Si phase fractions were also estimated by using data collected by 2D detector (HI-XRD), which gives a higher signal to noise ratio at the expense of the resolution. Even though the same samples were used for the experiments, surprisingly, different relative peak intensities of Al and Si phases were recorded, hence different phase fractions. The trend of phase fractions calculated using HR- and HI-XRD data (compared in Table 2) among samples is the same; but absolute values change, especially with respect to the specimens with Si in nanometric form. In particular, the amount of segregated Si phase was found to be around 3 % using the 2D detector and 6 % using the high-resolution setup. This discrepancy is attributed to the fact that reliable intensities have to be recorded on both very intense and small peaks at the same time. This requires the detector response to be linear on a very wide dynamic range, otherwise the intensities of the main Al peaks may be underestimated, leading to the overestimation of the Si phase amount. This is the case of the scintillators used to record HR-XRD data, whose Si phase fractions are, therefore, not reliable on an absolute scale. On the other hand, HI-XRD provides a more reliable response on the full intensity scale, thus leading to phase fractions closer to the real value.

The rapid solidification and cooling involved in L-PBF leads to the formation of an extended solid solution of Si in Al that is partially lost after direct aging, suggesting the precipitation of Si in addition to the strengthening precipitates. Solution annealing followed by water quenching leads to almost double amount of Si phase compared to that detected in the as built condition.

The thermal treatments were also responsible for a change in macro-strain within the Al matrix, as shown by data reported in Table 2. The macro-strain e is defined as the shift of observed *d*-space (d_o) with respect to the d-space expected for the lattice parameter computed by Rietveld refinements (d_c) [34].

$$e = \frac{(d_o - d_c)}{d_o} \qquad \text{eq.4}$$

Marked peak shift was detected, especially for the (200) of the AB sample toward lower angles, corresponding to a tensile strain that was evaluated to be 2.88E-4. T5 temper brought a significant reduction in the macro-strain level. Thus, direct aging is not only able to increase hardness and strength of metal (see Table 1), but it is also useful to partially release residual stresses. Moreover, as expected, solution treatment performed at 540 °C for 1 h was also able to decrease efficiently the macro-strain that dropped to 1.36E-04. Artificial aging at 160 °C for 4 h performed on the solution treated samples was responsible for a further decrease in macro-strain, due to release of stresses generated by water quenching from 540 °C. It is worth mentioning that the measured macro-strain has not to be considered as representative of the overall L-PBF part, but only of the investigated region (that is the same for all the investigated samples). However, it is interesting to monitor macro-strain values to evaluate the capability of the different heat treatment schedules to reduce residual stress. This also applies for the strain distribution evaluated by XRD-CT that are presented in the next section.

XRD-CT analysis

In order to assess a spatially resolved structural information, XRD-CT analysis was performed. Although the voxels size is rather coarse with respect to particle size to extract information about Si and Al phase morphologies, such an experiment can provide valuable information about the strain field in α-Al phase. The macro-strain is reported in Figure 2 for each specimen, in sections with diameter of 0.5 mm taken with a vertical step of 25 μm. It turns out that the highest macro-strain (in tension) occurs for the AB specimen, followed by T5. The AB specimen displays the largest macrostrain values among the specimens investigated. In addition, it shows macrostrain fluctuations within each section, with regions, in the order of ~100 μm, with much lower values. The thermal history of materials processed by LPBF is rather complex and not homogeneous within the printed part [35]. Thus, fluctuations in macrostrain are related to different gradients of temperature that are generated in the different areas of the melt pool and surrounding materials. Much lower macrostrain values are observed for ST and T6.

The macrostrain evolution is consistent with the values from HR-XRD reported in Table 2. Indeed, XRD-CT provides a spatial resolved information of macrostrain, while HR-XRD gives an information that is averaged over the full volume of the sample.

Tomography was exploited also as an alternative method to estimate the concentration of segregated Si phase by Rietveld refinement, the results are reported in Table 2. By considering again the central region of the specimens, estimated phase fractions are consistent with those calculated by HI-XRD data. Rietveld refinements performed on patterns extracted from different regions of the samples revealed a variation of about 1.0 % wt. across the material. The values reported in Table 2 are the average Si phase fractions

mediated over different regions of the specimen. The standard deviation (~0.5 % for each specimen) can be taken as a reliable estimate of the uncertainty.

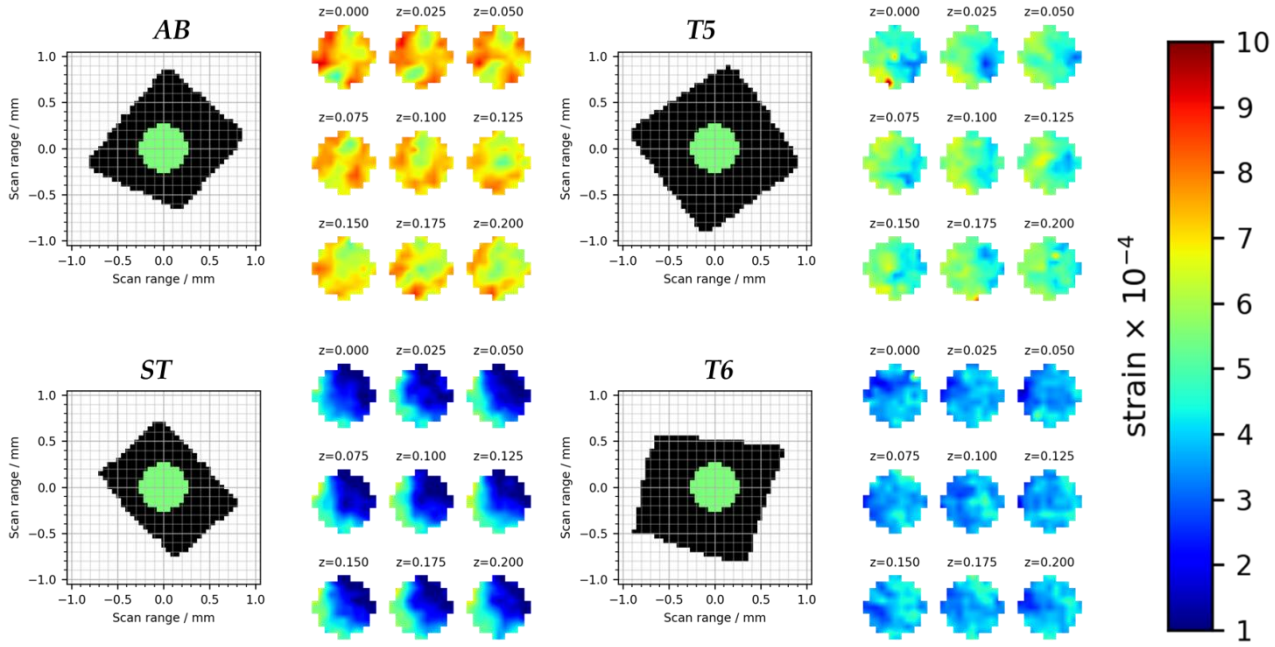

Figure 2 Macro-strain variation within the inner section for each specimen, recorded at different heights z. The inset on the left correlates the region of interest with respect to the shape of the sample, with a diameter of 500 μm. The magnitude of the strain, reported in the right, is taken as average over the first five reflections.

LOM, FEG-SEM, and TEM analyses

Figure 3 shows the microstructure evolution of the AlSi7Mg produced by L-PBF alloy when subjected to different thermal treatments. In Figure 3a, an optical micrograph of the section parallel to the building direction of an as built sample shows a microstructure made by solidified melt pools, common features found in Al-Si alloys produced by L-PBF [1]. Coarse columnar grains grow across adjacent melt pools parallel to the built direction (i.e. along main temperature gradient). At higher magnifications, the TEM images of Figure 3b and Figure 3c reveal that grains are composed of primary α-Al cells with the same crystallographic orientation, which are in the range 300-800 nm. The Al cells are surrounded by fine eutectic silicon particles, which are about 10 nm in size. The size of the Si particles is in good agreement with the results achieved by XRD analysis. Si nanoparticles occasionally precipitate in the inner part of cells, as pointed out by blue arrows in Figure 3c. The precipitation of Si nanoparticles in the middle of cells is reasonably attributed to the recalescence due to the solidification of supercooled liquid, as explained for AlSi10Mg by Marola et al. [27] or to the heat conducted from nearby laser tracks. Fig. 3d displays the SAED pattern along

the $[100]_{Al}$ zone axis corresponding to the area shown in Fig. 3c. Besides the main spots of the Al crystal, one can see a ring (see blue arrow), corresponding to (111) Si reflections. A ring is observed rather than single spots, as many nano-sized Si crystals, randomly oriented, diffracted the electron beam. The next Si rings are not observed because they have lower intensity. Another spot is observed, not belonging to Al or Si phases, as it occurs at a different values of 2θ (see red arrow). Its position is consistent with the (124) reflection of the β-Fe intermetallic phase, however, the very small fraction of this phase prevented a complete analysis.

In Figure 3e, the TEM image of the alloy directly aged from the as built condition is reported. Artificial aging performed at 160°C leads to a slight coarsening of the Al cells and to the rearrangement of Si nanoparticles. At higher magnification (Fig. 3f) it is possible to notice an abundant precipitation of lath-shaped particles with an average length of about 20 nm, homogenously distributed within the α-Al cells and aligned along the three orthogonal $<100>_{Al}$ directions (the black dots are the cross sections of precipitates lying parallel to the $[100]_{Al}$ zone axis). They are consistent with morphology and orientation of metastable β'' ($Mg_4Al_3Si_4$) precipitates responsible for strength increase in Al-Si-Mg alloys [36]. These precipitates are small and coherent with the Al matrix [37], and they are hardly detectable by bulk powder diffraction.

Consistently with XRD analysis, it is confirmed that extended supersaturated solid solutions are formed in Al-Si-Mg alloys processed by L-PBF, which can give rise to precipitation hardening by direct aging from the as built condition. The opportunity to perform aging by skipping solution treatment allows preserving the refined microstructure typical of as built material and to achieve higher strength and hardness (see Table 1) due to precipitate formation. The optical and SEM micrographs of Figure 3g and Figure 3h show the microstructure of ST samples. Grains with a size in the range 5-25 μm and coarse particles with dark contrast, which revealed to be Si particles, are noticeable. The size of Si particle is in the range of a few micrometres. Fe-rich particles were also occasionally found in the matrix (Figure 3i). In good agreement with XRD analysis, most of them have needle-like shape, typical of the β-Al_5FeSi phase, which is known to be detrimental for both fracture and impact toughness of the alloy when found as coarse intermetallics in cast alloys [26].

Therefore, the increased mechanical properties of the T5-specimens as compared to those of the T6-specimens can be attributed to the refined microstructure of the directly aged material. Indeed, both the as built and the solution treated materials showed increased strength due to artificial aging, but the drop in material hardness, due to microstructure coarsening of both Al grains and Si phases induced by solution treatment could not be fully compensated by the artificial aging.

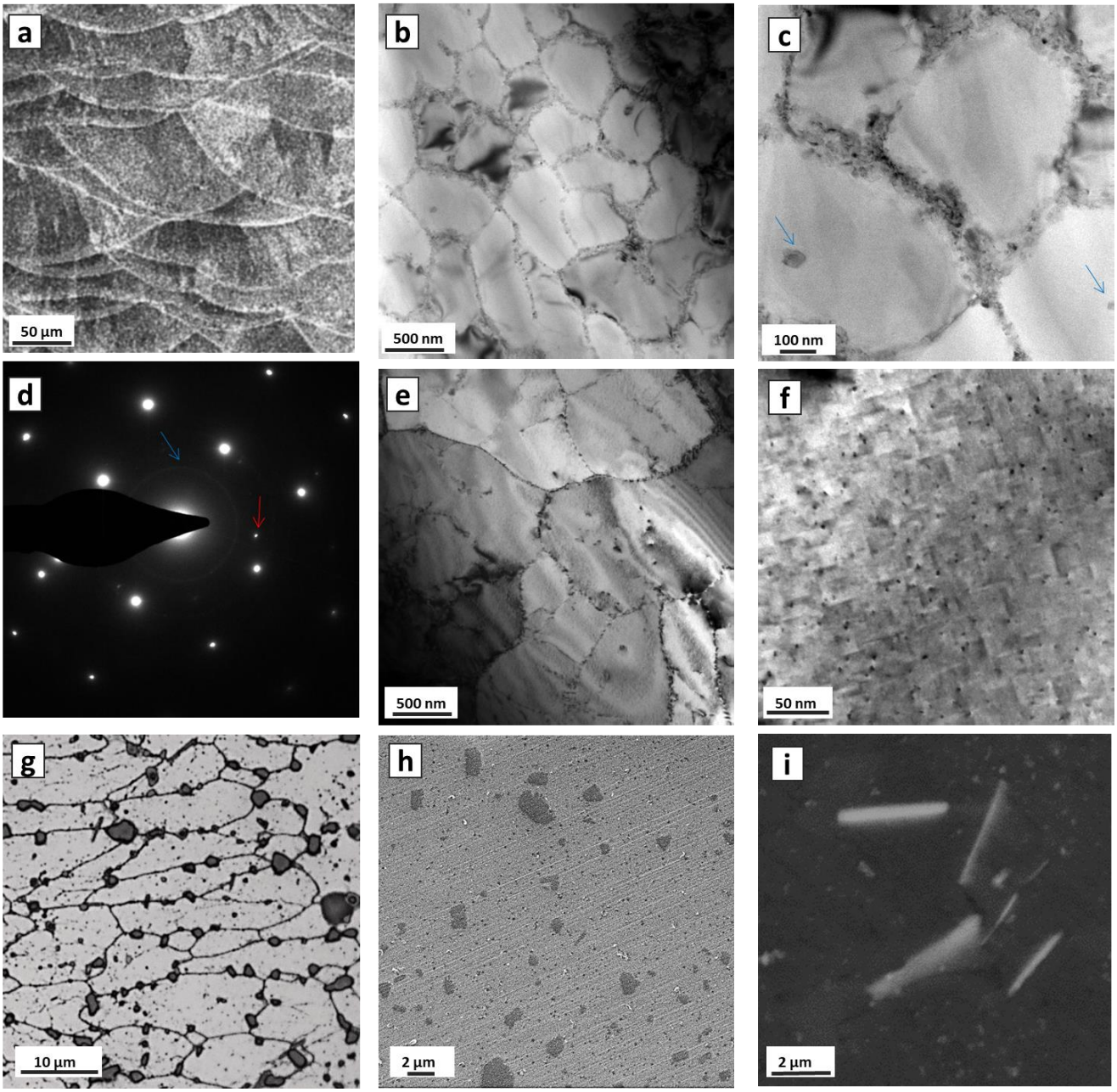

Figure 3 (a) LOM image of as built A357 alloy after electrolytic etching with Barker's solution (section parallel to the building direction); (b) and (c) TEM images of as built A357 alloy, the blue arrows point out Si nanoparticles found in the core of cells; *(d) SAED pattern related to the sample area of figure c, the blue arrow indicates ring to Si nanocrystals, the red arrow indicate a spot of a precipitate; (e) and (f) TEM images of A357 alloy directly aged from the as built condition; (g) Optical micrograph of solution treated sample; (h) and (i) SEM image of solution treated sample.*

Conclusions

We investigated the microstructure and macro-stress evolution in AlSi7Mg alloy produced by laser powder bed fusion and treated according to different routes by means of synchrotron powder diffraction, diffraction contrast tomography and electron microscopy. The as built alloy shows the higher lattice contraction and the lower amount of Si phase compared to other investigated conditions, thus suggesting a higher content of solute Si. The saturation degree decreases by artificial aging and by solution treatment. The eutectic Si has nanometric size in the as built material and grows significantly after solution treatment. A similar behaviour is shown by β-Al_5FeSi phase. Traces of the π-$Al_8FeMg_3Si_6$ intermetallic were observed after solution treatment. Direct aging was able to generate a fine dispersion of β'' precipitates in the primary Al solidification cells. The thermal treatments have also an evident effect on the $(200)_{Al}$ macro-strain measured from XRD-HR data, which is higher for the as built alloy and decreases after direct aging and even more after solution treatment followed by aging. This was confirmed by XRD-CT, which provided a spatial resolved structural information and was used as alternative tool to quantify the distribution of Si and Al phases.

To conclude, we discussed the quantification of the Si content in Al matrix, and consequently the residual Si through XRD. While a qualitative information about Si solubility can be easily accessed by the observed shift of XRD peaks towards higher angles, a quantification analysis is less trivial as the literature models should be adjusted to the composition of interest for each study. The estimate of the correct fraction of segregated Si can be easily affected by the instrument characteristics, as correct absolute intensities must be recorded on a wide intensity range.

Acknowledgement

The authors acknowledge the ESRF for provision of beam time and Dr. A. Vamvakeros for helping in XRD-CT analysis.

The present research was also supported by the Italian Ministry for Education, University and Research (MIUR) through the project "Department of Excellence LIS4.0" (Integrated Laboratory for Lightweight and Smart Structures).

Data Availability statement

The raw/processed data required to reproduce these findings cannot be shared at this time due to technical or time limitations.

References

[1] T. DebRoy, H.L. Wei, J.S. Zuback, T. Mukherjee, J.W. Elmer, J.O. Milewski, A.M. Beese, A. Wilson-Heid, A. De, W. Zhang, Additive manufacturing of metallic components – process, structure and properties, Prog. Mater. Sci. 92 (2018) 112–224.

[2] C.D. Marioara, S.J. Andersen, H.W. Zandbergen, R. Holmestad, The influence of alloy composition on precipitates of the Al-Mg-Si system, Metall. Mater. Trans. 36A (2005) 691–702.

[3] K. K. Matsuda, Y. Sakaguchi, Y. Miyata, Y. Uetani, T. Sato, A. Kamio, and S. Ikeno, Precipitation sequence of various kinds of metastable phases in Al-1.0mass% Mg2Si-0.4mass% Si alloy, J. Mater. Sci. 35 (2000) 179-189.

[4] P.H. Ninive, A. Strandlie, S. Gulbrandsen-Dahl, W. Lefebvre, C.D. Marioara, S.J. Andersen, J.D. Friis, R. Holmestad, O.M. Løvvik, Detailed atomistic insight into the β" phase in Al–Mg–Si alloys, Acta Mater. 69 (2014) 126-134.

[5] R. Casati, M. Vedani, Aging Response of an A357 Al Alloy Processed by Selective Laser Melting, Adv. Eng. Mater. 21 (2019) 1800406.

[6] J. Zvoníček, D. Koutný, L. Pantělejev, D. Paloušek Development of Process Parameters for SLM Processing of AlSi7Mg Aluminum Alloy, Current Methods of Construction Design (2010) 515-524.

[7] L.Boniotti, S.Beretta, L.Patriarca, L.Rigoni, S.Foletti Experimental and numerical investigation on compressive fatigue strength of lattice structures of AlSi7Mg manufactured by SLM, International Journal of Fatigue 128 (2019) 105181.

[8] Z. Sajedi, R. Casati, M.C. Poletti, M. Skalon, C. Sommitsch, M. Vedani Thermo-mechanical Fatigue Behaviour of AlSi7Mg Alloy Processed by Selective Laser Melting. Euro PM2019 Conference (2019)

[9] Z. Sajedi, R. Casati, M.C. Poletti, M. Skalon, M. Vedani Thermal fatigue testing of laser powder bed fusion (L-PBF) processed AlSi7Mg alloy in presence of a quasi-static tensile load Materials Science and Engineering: A 789 (2020) 139617

[10] M.H. Nasab, S. Romano, D. Gastaldi, S. Beretta, M. Vedani Combined effect of surface anomalies and volumetric defects on fatigue assessment of AlSi7Mg fabricated via laser powder bed fusion Additive Manufacturing 34 (2020) 100918.

[11] J. Teixeira Oliveira de Menezes, E. M. Castrodeza, R. Casati Effect of build orientation on fracture and tensile behavior of A357 Al alloy processed by Selective Laser Melting, Materials Science and Engineering: A 766 (2019) 138392.

[12] M. Cabrini, S. Lorenzi, T. Pastore, C. Testa, D. Manfredi, F. Calignano, M. Lorusso, P. Fino Corrosion behavior of aluminum-silicon alloys obtained by Direct Metal Laser Sintering, Eurocorr 2017.

[13] P. Van Cauwenbergh, A. Beckers, L. Thijs, B. Van Hooreweder, K. Vanmeensel Heat Treatment Optimization via Thermo-Physical Characterization of AlSi7Mg and AlSi10Mg Manufactured by Laser Powder Bed Fusion (LPBF) Euro PM2018 congress, October, Bilbao – Spain

[14] M. Wang, B. Song, Q. Wei, Y. Shi Improved mechanical properties of AlSi7Mg/nano-SiCp composites fabricated by selective laser melting, Journal of Alloys and Compounds 810 (2019) 151926.

[15] M. Wang, B. Song, Q. Wei, Y. Zhang, Y. Shi Effects of annealing on the microstructure and mechanical properties of selective laser melted AlSi7Mg alloy Materials Science and Engineering: A 739 (2019) 463-472

[16] L. Wang, X. Jiang, Y. Zhu, X. Zhu, J. Sun, B. Yan An approach to predict the residual stress and distortion during the selective laser melting of AlSi10Mg parts, The International Journal of Advanced Manufacturing Technology 97 (2018) 3535–3546.

[17] J. Samei, M. Amirmaleki, M. Shirinzadeh Dastgiri, C. Marinelli, D. E. Green In-situ X-ray tomography analysis of the evolution of pores during deformation of AlSi10Mg fabricated by selective laser melting, Materials Letters 255 (2019) 126512

[18] Y. Nadot, C. Nadot-Martin, W. H. Kan, S. Boufadene, M. Foley, J. Cairney, G. Proust, L. Ridosz Predicting the fatigue life of an AlSi10Mg alloy manufactured via laser powder bed fusion by using data from computed tomography, Additive Manufacturing 32 (2020) 100899

[19] A. N. Fitch. The high resolution powder diffraction beam line at the ESRF. *J. Res. Natl Inst. Stand. Technol.* 109 (2004) 133–142.

[20] C. Dejoie, M. Coduri, S. Petitdemange, C. Giacobbe, E. Covacci, O. Grimaldi, P.-O. Autran, M. W. Mogodi, D. Šišak Jung, A. N. Fitch. Journal of Applied Crystallography 51 (2018) 1721–1733.

[21] G. Ashiotis, A. Deschildre, Z. Nawaz, J.P. Wright, D. Karkoulis, F.E. Picca, J. Kieffer, The fast azimuthal integration Python library: pyFAI, Journal of applied crystallography, 48 (2015) 510-519.

[22] G.B.M. Vaughan, R. Baker, R. Barret, J. Bonnefoy, T. Buslaps, S. Checchia, …, S.A Kimber, ID15A at the ESRF–a beamline for high speed operando X-ray diffraction, diffraction tomography and total scattering, Journal of Synchrotron Radiation 27 (2020)

[23] A. Vamvakeros, S.D. Jacques, M. Di Michiel, V. Middelkoop, C.K. Egan, R.J. Cernik, A.M. Beale, Removing multiple outliers and single-crystal artefacts from X-ray diffraction computed tomography data. Journal of Applied Crystallography, 48 (2015) 1943-1955.

[24] https://github.com/antonyvam/nDTomo

[25] G.K. Williamson, W.H. Hall, X-ray line broadening from filed aluminium and wolfram, Acta Metall. 1 (1953) 22-31.

[26] J.A. Taylor, Iron-containing intermetallic phases in Al-Si based casting alloys, Proc. Mater. Sci. 1 (2012) 19-33.

[27] S. Marola, D. Manfredi, G. Fiore, M.G. Poletti, M. Lombardi, P. Fino, L. Battezzati, A comparison of Selective Laser Melting with bulk rapid solidification of AlSi10Mg alloy, J. Alloys Compd. 742 (2018) 271–279.

[28] R. Casati, M.H. Nasab, M. Coduri, V. Tirelli, M. Vedani. Effects of Platform Pre-Heating and Thermal-Treatment Strategies on Properties of AlSi10Mg Alloy Processed by Selective Laser Melting, Metals 8 (2018) 954

[29] A. Bendijk, R. Delhez, L. Katgerman, Th. H. De Keijser, E. J. Mittemeijer, N. M. Van Der Pers. Characterization of Al-Si-alloys rapidly quenched from the melt. *Journal of Materials Science* 15 (1980) 2803-2810.

[30] H. A. Moreen, R. Taggart and D. H. Polonis, A Model for the Prediction of Lattice Parameters of Solid Solutions. *Met. Trans.* 2 (1971) 265.

[31] J. L. Murray, The Al−Mg (Aluminum−Magnesium) system. *Journal of Phase Equilibria* 3, 60 (1982).

[32] W. Li, S. Li, J. Liu, A. Zhang, Y. Zhou, Q. Wei, C. Yan, Y. Shi. Effect of heat treatment on AlSi10Mg alloy fabricated by selective laser melting: Microstructure evolution, mechanical properties and fracture mechanism. Materials Science and Engineering: A (2016) 663, 116-125.

[33] A. Kempf, K. Hilgenberg; Influence of sub-cell structure on the mechanical properties of AlSi10Mg manufactured by laser powder bed fusion. Materials Science and Engineering: A (2020) 776, 138976.

[34] I. C. Noyan, J. B. Cohen. *Residual Stress: Measurement by Diffraction and Interpretation*. New York: Springer-Verlag (1987).

[35] Y. M. Arısoy, L. E. Criales, T. Özel Modeling and simulation of thermal field and solidification in laser powder bed fusion of nickel alloy IN625, Optics & Laser Technology 109 (2019) 278-292.

[36] G. Asghar, L. Peng, P. Fu, L. Yuan, Y. Liu. Role of Mg2Si precipitates size in determining the ductility of A357 cast alloy, Materials & design 186 (2020) 108280.

[37] S. J. Andersen, H. W. Zandbergen, J. Jansen, C. Trholt, U. Tundal, O. Reiso The crystal structure of the β'' phase in Al‑Mg‑Si alloys, Acta Materialia 46 (1998) 3283-3298.